PHYSICAL REVIEW MATERIALS **8**, 073602 (2024)

Structure and thermodynamics of defects in Na-feldspar from a neural network potential

Alexander Gorfer,[1,2,3] Rainer Abart,[2] and Christoph Dellago[1]
[1]*Faculty of Physics, University of Vienna, Boltzmanngasse 5, 1090, Vienna, Austria*
[2]*Department of Lithospheric Research, University of Vienna, Josef-Holaubek-Platz 2, 1090, Vienna, Austria*
[3]*Vienna Doctoral School in Physics, University of Vienna, Boltzmanngasse 5, 1090, Vienna, Austria*

(Received 8 February 2024; revised 31 May 2024; accepted 2 July 2024; published 18 July 2024)

The diffusive phase transformations occurring in feldspar, a common mineral in the crust of the Earth, are essential for reconstructing the thermal histories of magmatic and metamorphic rocks. Due to the long timescales over which these transformations proceed, the mechanism responsible for sodium diffusion and its possible anisotropy has remained a topic of debate. To elucidate this defect-controlled process, we have developed a neural network potential (NNP) trained on first-principle calculations of Na-feldspar (albite) and its charged defects. This force field reproduces various experimentally known properties of feldspar, including its lattice parameters and elastic constants as well as heat capacity and DFT-calculated defect formation energies. A new type of dumbbell interstitial defect is found to be most favorable, and its free energy of formation at finite temperature is calculated using thermodynamic integration. The necessity of including electrostatic corrections before training an NNP is demonstrated by predicting more consistent defect formation energies.

DOI: 10.1103/PhysRevMaterials.8.073602

I. INTRODUCTION

Feldspar is the most abundant mineral in the Earth's crust and an important ingredient for ceramics [1]. It forms a solid solution between a sodium ($NaAlSi_3O_8$, albite), calcium ($CaAl_2Si_2O_8$, anorthite), and a potassium ($KAlSi_3O_8$, K-feldspar) end-member component. The most prominent feldspar groups are represented by the plagioclase ($NaAlSi_3O_8$, $CaAl_2Si_2O_8$) and the alkali feldspar ($NaAlSi_3O_8$, $KAlSi_3O_8$) solid solution series. At high temperatures typical for magmatic and metamorphic environments, both solid solution series show complete miscibility. Towards lower temperatures miscibility gaps open, and feldspars of intermediate composition tend to exsolve, typically producing lamellar intergrowth of feldspars with different compositions. The exsolution microstructures are of particular interest for reconstructing the thermal history of magmatic and metamorphic rocks [2,3]. In addition, elastic strain associated with exsolution microstructures may lead to pseudocleavage along the so-called Murchison plane, which may enhance the ice nucleation activity of exsolved feldspar making the corresponding aerosol particles potentially important players in the glaciation of clouds [4].

Exsolution of an initially homogeneous feldspar implies segregation of the different cations on the alkali and alkali earth sub-lattices, which occurs by intracrystalline diffusion. Due to the long timescales over which diffusive phase transformations in feldspar proceed, the underlying diffusion mechanisms and their possible anisotropy still hold unresolved questions, such as the recently discussed systematic differences between experimentally determined Na-K interdiffusion coefficients and those theoretically predicted from measured tracer diffusion coefficients [5–9].

On the computational side, the diffusion of alkali defects in feldspar has been studied with kinetic Monte Carlo simulations [10–12] using empirical rate constants. Interatomic potentials capturing all constituent elements of the material and its defects are needed for studying the microscopic mechanism of diffusion without referring to laboratory experiments. It has been demonstrated that classical force fields are capable of reproducing the overall properties of various kinds of silicates and aluminosilicates [13], and they have been applied for studying diffusion barriers of sodium vacancies in Na- and K-feldspar [14]. These classical force fields, however, fall behind density functional theory (DFT) methods, which have been demonstrated to predict various properties of feldspar accurately [15]. Yet DFT and other *ab initio* methods are computationally considerably more expensive than classical force fields, drastically limiting the accessible system sizes and simulation times. Recently, machine learned force fields (MLFFs) have been shown to offer accuracy comparable to first-principle electronic-structure calculations at a cost comparable to that of classical force-field calculations [16,17]. Such MLFFs have already been used to study a vast array of systems ranging from organic molecules and inorganic crystals to surfaces, aqueous systems, and biomolecules [18–20]. In particular, MLFFs have been used for studying diffusion in lead and cadmium telluride [21], and an MLFF for studying ice nucleation on K-feldspar has been developed recently [22].

In this paper we address sodium feldspar albite ($NaAlSi_3O_8$), the conventional unit cell of which contains four formula units in a $C\bar{1}$ spacegroup and is illustrated in

---

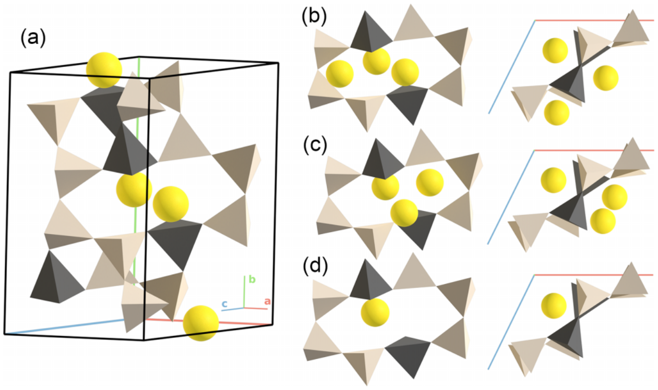

FIG. 1. Unit cell of albite (a) and three possible defects (b)–(d). White tetrahedrons are $[SiO_4]^{-4}$, black ones are $[AlO_4]^{-5}$, and yellow spheres are Na^+. The defects are shown relative to the central eight-membered ring of tetrahedrons. The three defects, shown in side and top view, are (b) the $Na^+_{(00\frac{1}{2})}$ interstitial defect, (c) the dumbbell interstitial Na^+_{DB}, and (d) the vacancy V^-_{Na}. The configurations shown above were relaxed using NNPw/corr. Note that the unit cell used here is shifted by $(\frac{1}{2}\frac{1}{2}\frac{1}{2})$ with respect to the origin of the unit cell usually used for feldspar.

Fig. 1(a). We develop a Behler-Parrinello-type neural network potential (NNP) for sodium feldspar, paying particular attention to an accurate representation of defects. Trained on a reference data set obtained with DFT using the PBE functional [23], our NNP accurately reproduces forces and energies, and it can be used to carry out extensive molecular dynamics simulations. We demonstrate its applicability by computing the heat capacity as well the elastic constants and the geometry of the unit cell of Na-feldspar over a wide range of temperatures, finding good agreement with experimental data. In addition, we investigate the structure and diffusion of charged interstitial and vacancy defects, taking electrostatic finite-size corrections into account. Such Frenkel pairs, consisting of Na^+ interstitials and Na^+ vacancies, are expected to be the majority carrier of alkali defects, since Schottky defects are energetically improbable due to the high Si-O bonding energy [24]. The computational efficiency of the NNP allowed us to determine the defect formation free energy, and from it the defect concentrations for temperatures from 0 K up to 1400 K using thermodynamic integration. Furthermore, our simulations revealed a new interstitial configuration, in which two Na^+ cations share an alkali lattice site [Fig. 1(c)]. This dumbbell-like defect is thermodynamically more favorable than the $Na^+_{(00\frac{1}{2})}$ interstitial shown in Fig. 1(b) that was considered previously [25]. Interestingly, the energetically favorable orientation of the dumbbell changes discontinuously at a temperature of about 752 K. The current version of our NNP can be used to model sodium feldspar, but it can be readily extended to potassium feldspar and the solid solution of alkali feldspar by retraining it with an extended traning set.

The remainder of the paper is organized as follows. In Sec. II we describe the computational methods used in our work, including the preparation of the reference data and the training of the NNP. Results are presented and discussed in Sec. III, and conclusions are provided in Sec. IV.

II. METHODS

A. *Ab initio* calculations

All our DFT calculations were performed using the Vienna Ab-initio Simulation Package (VASP) [26–28] with the projector augmented wave method [29] utilizing the Perdew-Burke-Ernzerhof (PBE) exchange-correlation functional [23]. The conventional cell containing four formula units of $NaAlSi_3O_8$, initially constructed using experimental data of Armbruster and colleagues [30] with Al always kept at the T_1O-sites, was sampled using a $6\times4\times6$ Γ-centered k-point mesh. The same k-point density in the Brillouin zone was kept across all calculations, and the energy cutoff was set to 560 eV. The convergence criteria were 10^{-5} eV Å^{-1} for the self-consistent cycle and 10^{-3} eV Å^{-1} for ionic relaxations. When varying the number of electrons, a neutralizing jellium background was included.

B. Defect formation energies and their correction

To determine the equilibrium concentrations of point defects in Na-feldspar it is necessary to calculate defect formation energies. Since vacancies and interstitials carry a charge, their energy in a periodicically replicated system suffers from strong finite-size effects that require proper corrections. For charged defects in a periodic supercell the defect formation energy is given by [31,32]

$$E_{\text{form}} = (E[\text{Defect}] + E_{\text{corr}}[\text{Defect}]) - E[\text{Bulk}] - \sum_i n_i\mu_i + q(\epsilon_{\text{VBM}} + \Delta E_{\text{FL}}). \quad (1)$$

Here E[Defect] is the total energy obtained from a supercell calculation containing the defect and E[Bulk] is the total energy of the pristine supercell. The term E_{corr}[Defect] is a finite-size correction explained in more detail below. The integer n_i is the number of atoms of type i added to $(n_i > 0)$ or removed from $(n_i < 0)$ the system, and μ_i is the corresponding chemical potential in the reservoir with which the atoms are exchanged. The last term in the equation represents the energy required to introduce or remove the electronic charge q, which is $q = -1$ for Na^+ vacancies and $q = +1$ for Na^+ interstitials. Here ϵ_{VBM} is the electron energy at the valence band maximum (VBM) and ΔE_{FL} the Fermi level. As is common for 0 K DFT calculations, we identify $\Delta E_{\text{FL}} = 0$.

As mentioned above, when calculating the formation energy of charged defects in the supercell approach one invariably introduces interactions between the defect, its periodic images, and the neutralizing background charge, necessitating the correction E_{corr}. The most important contribution to this correction is the spurious Coulomb interaction, which remains significant for any practical supercell size. Several methods exist to subtract this interaction from the defective supercells. Apart from the extrapolative scheme, in which the defect formation energy is determined for a sequence of supercells of increasing size whose limiting value can be identified with the dilute limit, there have been major developments in for-

TABLE I. Ionic (ϵ^0) and electronic (ϵ^∞) contributions to the static dielectric tensor $\epsilon_{ij}(0)$ of Na-feldspar computed in GGA. To compare with experimental data, we estimated the dielectric constant of a polycrystalline sample by $\epsilon_{\text{poly}} = (\lambda_1 + \lambda_2 + \lambda_3)/3$, where $\lambda_1, \lambda_2, \lambda_3$ are the eigenvalues of the dielectric tensor. The result is an ϵ_{poly} equal to 6.18 vs values of 7 and 8 from experiments of Olhoeft [36] and Jones *et al.* [14], respectively.

	ϵ^∞	ϵ^0	Σ
ϵ_{xx}	2.404	2.602	5.006
ϵ_{yy}	2.441	4.664	7.105
ϵ_{zz}	2.415	4.019	6.434
ϵ_{yz}	−0.005	−1.576	−1.581
ϵ_{zx}	−0.007	−0.273	−0.280
ϵ_{xy}	0.001	0.110	0.111

mally removing the electrostatic interactions by corrections [33]. Here we use the correction of Kumagai and Oba, which was introduced as the "extended FNV scheme" in [33]. The effects of microscopic screening are inferred by the atomic site electrostatic potentials of the pristine system and of the system with the defect after ionic relaxation. To compute this correction, we first determined the dielectric tensor of albite using DFT perturbation routines in VASP [34]; see Table I. Then we calculated the correction from pristine and relaxed defective supercells of the various systems (listed in Table IV) using the Spinney package [35]. The potentials involved in the correction are provided in the Supplemental Material [77].

C. Architecture of the NNP committee

In this work the potential energy surface is represented by artificial neural networks as proposed by Behler and Parrinello in 2007 [16]. Local atomic environments are expressed by radial and angular atom-centered symmetry functions with a cutoff of 6 Å. The atomic feed-forward neural networks consist of an input layer containing 256 nodes in the case of aluminum, 272 for silicon, 273 for sodium, and 276 for oxygen. All four networks further consist of two hidden layers with 25 nodes each and one single output node. The weights and biases were initialized randomly and optimized using a parallel Kalman-Filter [37] to minimize the root-mean-squared deviation between predicted energies and forces and the reference values. The n2p2 package [38] was used to train the potentials and to interface them with the molecular dynamics simulation package LAMMPS [39].

We used several independent NNPs, trained with different initial weights, in a committee machine, i.e., predictions for a certain configuration A are calculated as an average over N independent predictions $\mathbf{y}_i$:

$$\bar{\mathbf{y}}(A) = \frac{1}{N}\sum_i \mathbf{y}_i(A). \tag{2}$$

For all our calculations we used the committee method implemented in n2p2 by Kývala *et al.* [40] with a committee size of $N = 4$. Committee machines are known to increase the precision of machine-learning models and reduce overfitting, and they have been used to improve predictions of various physical properties [41,42]. Furthermore, the variance $\sigma(A)$ of the individual predictions can serve as a measure for the uncertainty of the averaged prediction $\bar{\mathbf{y}}(A)$ [43–45]. As explained below, we use this uncertainty in our active learning strategy for the generation of the reference data.

D. Data set generation

1. Active learning

To generate the data set needed to train and test our NNP, we used a two-stage strategy. In the first stage, we carried out an on-the-fly machine learning simulation using VASP [46,47]. In this approach, an *ab initio* molecular dynamics simulation is started and a Gaussian process regression (GPR) model is continuously trained on the energies and forces computed from DFT. As the simulation proceeds and the accuracy of the GPR model improves, the expensive electronic structure calculations are successively replaced by the computationally inexpensive GPR model. DFT calculations are carried out only if the accuracy of the GPR model, as determined from Bayesian error estimation, falls below a given threshold. Since with time the relevant part of configuration space gets explored by the simulation, fewer and fewer DFT calculations become necessary, speeding up the simulation considerably.

With this on-the-fly approach, a relaxed $2\times1\times2$ supercell was driven from 0 to 1300 K in 20 000 steps at atmospheric pressure in the NPT ensemble. In these and all subsequent on-the-fly simulations a timestep of 1.5 fs was used. Whenever an electronic structure calculation was carried out, the respective configuration together with its energy and forces was added to the reference data set. The simulation was continued at 1300 K until there were no new uncertain configurations added to the reference set for a span of at least 20 000 steps. The same procedure was repeated for a relaxed $2 \times 1 \times 2$ supercell in which a sodium atom was introduced and an electron removed to create an Na_i^+ interstitial defect. This system took the longest to reach acceptable predictive accuracy at 1300 K with 100 000 steps necessary. Finally, the procedure was carried out for a relaxed supercell in which a sodium was removed and an additional electron introduced to create a $\mathrm{V}_{\mathrm{Na}}^-$ vacancy. Throughout all of these simulations a total of 220 000 time steps were carried out, long enough such that several intracrystalline hopping events of the defects were already observed therein. Of the total number of timesteps, 1679 were calculated using forces determined *ab initio*.

While MD simulations can be carried out with the GPR model directly, it is known that NNPs are superior to GPR models in terms of speed. In the second stage of our strategy, we have therefore used energies and forces computed *ab initio* for the 1679 configurations collected on the fly to train an NNP. More specifically, a committee of four neural-network potentials (their architecture is given in Sec. II C) was trained with n2p2. The committee was then used to run MD simulations with $2\times2\times2$ supercells in a pristine system and with interstitial or vacancy defects in the NPT ensemble up to 1400 K with a time step of 1 fs. Every fifth time step the force uncertainty for each atom was determined. Since the force uncertainty is a local quantity in contrast to the uncertainty of the total energy, we expect it to be a more suitable measure of uncertainty. Configurations where any atomwise force uncertainty was above the threshold of five times the RMSE (analogous to Ref. [48]) were collected. Configurations that were at least 100 fs apart were recalculated with VASP and put into the reference data set. With this augmented reference data set a new committee was trained and the process was repeated. After four such iterations the committee produced a low rate of uncertain configurations and the procedure was stopped. A total of 670 additional DFT calculations were necessary in this procedure. An increase in the required training set size between the initial GPR model of VASP, and the final NNP had to be expected as GPR models are known to require less data than NNPs; see, e.g., Ref. [49]. In total, the training set contained 2351 configurations with energies and forces.

To test the prediction of the NNP, a test set was created by sampling random structures throughout all simulations. In addition, with the final committee, MD simulations exceeding 3 ns of the $2\times2\times2$ systems were performed, and 400 structures each of the pristine system and the system containing an Na_i^+ as well as the system with a V_Na^- were calculated with first principles and added to the test set. In total, the test set contained 1302 configurations with energies and forces. Let us denote the data set obtained so far by

$$\mathcal{A}_1 = \{A_i, (E_i, \mathbf{f}_i)\},$$

where A_i are the configurations, and E_i and $\mathbf{f}_i$ are the corresponding potential energies and forces, respectively, obtained in the supercell calculations.

2. *Including electrostatic corrections in the data set*

The data set $\mathcal{A}_1$ does not contain the finite-size corrections stipulated in Eq. (1) to calculate defect formation energies. Since machine-learning force fields allow us to go to large system sizes at which the spurious long-range Coloumb interaction between a charged defect and its periodic images may actually become negligible, it was not clear if electrostatic finite-size effects should be included or corrected for in the reference data. To ensure a proper force field that treats these charged defects consistently, we created a second labeled data set:

$$\mathcal{A}_2 = \{A_i, (E_i + E_\mathrm{corr}(A_i), \mathbf{f}_i)\},$$

where $E_\mathrm{corr}(A_i)$ is the electrostatic finite-size correction that depends on the configuration A_i. That is, corresponding to the system size and defect type, we add the correction before training to incorporate it into the neural-network potential. Apart from this, the configurations of $\mathcal{A}_2$ are identical to those of $\mathcal{A}_1$. Note that the Kumagai-Oba correction allows us to include effects of lattice relaxations into the microscopic screening. We then identified $E_\mathrm{corr}(A_i)$ for any finite temperature configuration A_i by the correction of the relaxed system of the same supercell-size and defect type.

E. Heat capacity, elastic constants, and phonons

To assess the performance of the NNP compared to its DFT reference as well as to experimental data we calculated the elastic constants and heat capacity. To calculate the elastic constants at the DFT level we used displacements of the box and of the ions with a step size of 0.015 Å for the stress-strain relationship [50] implemented in VASP. To calculate the elastic constants with NNPs we used box displacements with a relative deformation magnitude of 2×10^{-4} for the stress-strain relationship as implemented in LAMMPS/examples/ELASTIC. The isochoric heat capacity C_V was determined through the phonon density of states obtained using the phonopy [51] codes for DFT and the NNPs respectively. To compare with experiments the isochoric heat capacity C_V was transformed to the isobaric heat capacity C_P through the relation $C_P = C_V + TV\alpha^2K$. Values for the thermal expansion coefficient α were calculated from the temperature dependence of the volume that we obtained from thermodynamic integration (next section) and the bulk modulus K was calculated using the Voigt-Reuss-Hill average of the elastic constants. A finite temperature anharmonic renormalization of the phonon band structure was performed using normal-mode decomposition [52] as implemented in dynaphopy [53].

F. Thermodynamic integration and parallel tempering

One of the goals of this work is to compute the equilibrium concentrations of interstitial and vacancy defects as a function of temperature. We accomplish this by determining the free energy of formation of Frenkel pairs $G_\mathrm{FP}(T)$, from which their concentration follows [54]

$$C_\mathrm{FP}(T) = \exp\left(\frac{-G_\mathrm{FP}(T)}{2k_\mathrm{B}T}\right). \tag{3}$$

The formation free energy $G_\mathrm{FP}(T)$ is calculated via thermodynamic integration following Cheng and Ceriotti [55] using i-PI [56] and LAMMPS [39]. To achieve sufficient sampling also at low temperatures, we employ a parallel replica scheme [57] coupling isothermal-isobaric MD simulations at different temperatures, from 100 K up to the melting point of 1400 K [58–60]. Note that this approach takes into account full anharmonic effects, which can become relevant at the higher temperatures [61,62]. Details about this free energy calculation are included in the Supplemental Material [77].

III. RESULTS

A. Performance of the neural network potentials

The accuracy of the neural network potential committees trained without charge corrections (NNPw/o) and with charge corrections (NNPw/corr) was first assessed by comparing the predicted forces and total energies with the reference data for the test set. The test set of NNPw/corr was appropriately shifted just like its training set $\mathcal{A}_2$.

As can be seen in Fig. 2 and Table II, the NNP predictions are close to the reference data with an accuracy that is on par with similarly constructed neural-network potentials [21] or other types of machine-learning force fields [47]. In particular, the errors for NNPw/o and NNPw/corr are essentially the same.

B. Heat capacity, elastic constants, and unit cell

In Fig. 3(a) the elastic constants obtained from DFT as well as with the NNP with (NNPw/corr) and without (NNPw/o) corrections are shown. The figure also includes results of DFT

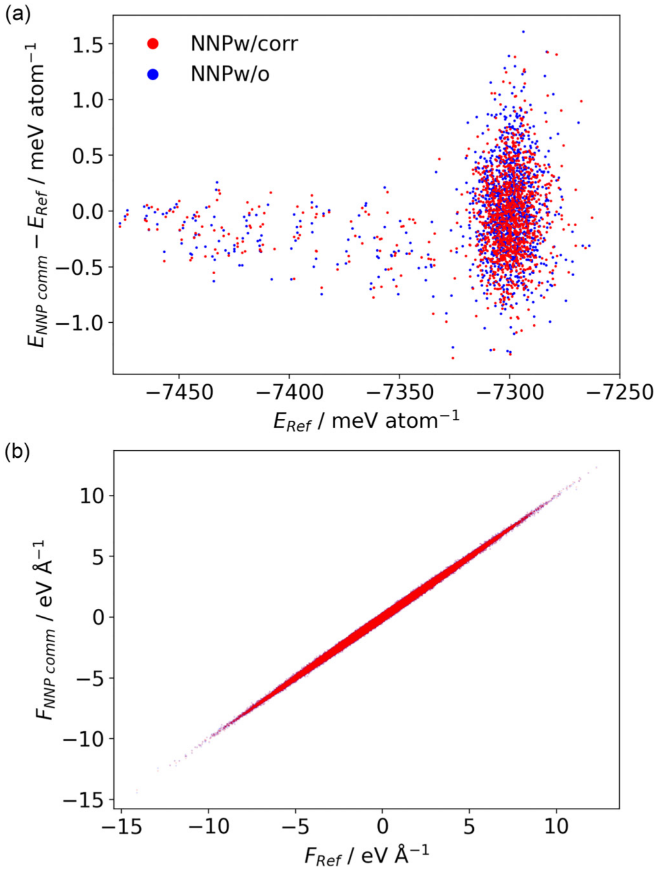

FIG. 2. (a) Deviation of the predicted energy from the reference energy vs. reference energy for NNPw/o and NNPw/corr; (b) predicted forces vs reference forces for NNPw/o and NNPw/corr.

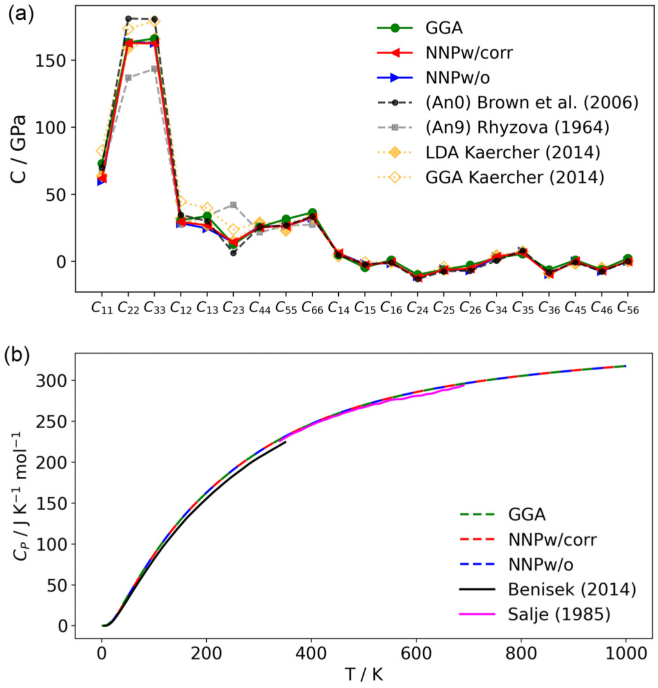

FIG. 3. (a) Elastic constants obtained from the NNP, DFT, and experiments. We use the orientation convention $\mathbf{Z}\|\mathbf{c}$, $\mathbf{Y}\|\mathbf{a}\times\mathbf{c}$, $\mathbf{X}\|\mathbf{Y}\times\mathbf{Z}$). (b) Isobaric heat capacity C_P vs temperature.

calculations of Kaercher *et al.* [15] and experimental results of Brown *et al.* [63] and Rhyzova [64]. Note that in the calculations of Kaercher *et al.* [15] the volume of the system was fixed at the experimental density during relaxation, making their results correspond to a high pressure. The results for NNPw/o and NNPw/corr almost fall on top of each other and both reproduce the DFT generated constants well overall. For the bulk modulus, the Voigt-Reuss-Hill average yields 54.0 GPa in the case of the NNPs and 58.7 GPa if referring to DFT. The latter is closer to the bulk modulus of 59.5 GPa as reported from measurements of Brown *et al.* [63].

In Fig. 3(b) the isobaric heat capacity obtained from DFT, NNPw/o, and NNPw/corr and the experiments of Benisek *et al.* [65] and Salje *et al.* [66] are shown. The heat capacities we obtained with the three methods trace Salje's data, which are marginally higher than Benisek's experiments. The phonon band structure and DOS that is used to calculate the heat capacity for the NNPw/corr are shown in the Supplemental Material Fig. S-14 [77].

In Table III we list the unit cell parameters obtained from DFT, NNPw/o, and NNPw/corr as well as the experimental results of Brown *et al.* [63]. As is common with GGA-DFT, the lattice parameters are slightly overestimated, and this is reproduced in both NNPs. In Fig. 4 we plotted the change in unit cell dimensions as a function of temperature for the NNPw/corr. As can be inferred from the figure, the lattice parameters increase anisotropically with temperature. The change of the box angles is in the correct direction as feldspars become more monoclinic as temperature increases [67]. The thermal expansion coefficient that follows from Fig. 4 ranges from 3.3×10^{-5} between 0 and 100 K to 4.7×10^{-5} between 1300 and 1400 K. This compares reasonably well to experimental data which range from 3.0×10^{-5} [68] to 4.6×10^{-5} [69] and from 2.5×10^{-5} at 298 K to 3.4×10^{-5} at 900 K for a fit of Tribaudino *et al.* [70]. The whole temperature

TABLE II. Root-mean-squared errors for the test set obtained from the committee trained without charge correction (NNPw/o) and and with charge corrections (NNPw/corr).

RMSE	NNPw/o	NNPw/corr
$\Delta E\ [\frac{\text{meV}}{\text{atom}}]$	0.40	0.39
$\Delta F\ [\frac{\text{eV}}{\text{Å}}]$	0.065	0.065

TABLE III. Unit cell parameters of Na-feldspar for the experiment of Brown and coworkers [63] and fully relaxed unit cells of GGA and the two NNPs.

	a [Å]	b [Å]	c [Å]	α [deg]	β [deg]	γ [deg]
GGA	8.260	12.933	7.250	94.210	116.489	87.555
NNPw/corr	8.254	12.929	7.250	94.171	116.474	87.556
NNPw/o	8.248	12.935	7.250	94.165	116.471	87.573
Brown *et al.*	8.137	12.786	7.158	94.253	116.605	87.756

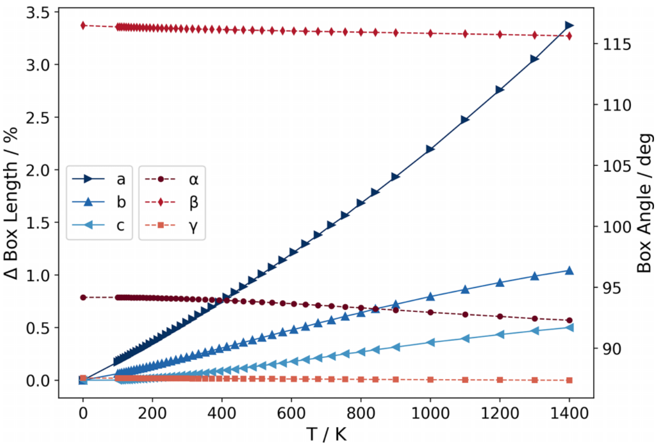

FIG. 4. Percent changes of the edge lengths a, b, and c (left y axis) of the unit cell as a function of temperature with respect to the unit cell at 0 K for NNPw/corr. Also shown are the angles α, β, and γ of the unit cell (right y axis).

dependence of the thermal expansion coefficient is shown in the Supplemental Material in Fig. S-10 [77].

C. Defect formation energies at 0 K

In the feldspar structure illustrated in Fig. 1(a) an interstitial atom can occupy only a restricted number of positions. We started by placing a sodium cation at the $(0, 0, \frac{1}{2})$ position, as proposed by Petrovic [25], and relaxed the system. This interstitial is refered to as $\mathrm{Na}^{+}_{(00\frac{1}{2})}$ and is shown in Fig. 1(b). In this configuration, the inserted cation lies on the same (010) plane as its neighboring sodium ions, to which it has a large separation. The two nearest sodium neighbors are 4.17 Å away and the two next nearest are at a distance of 4.34 Å, such that the defect is at an electrostatically favorable position as argued by Petrovic. While this defect is mechanically stable at low temperatures, on heating the system as described in Sec. II D 1 we observed that at a temperature of roughly 600 K the defect transitions to the dumbbell-type defect $\mathrm{Na}^{+}_{\mathrm{DB}}$ in which two Na^{+} share a single alkali lattice site, as shown in Fig. 1(c). The reverse transition, from dumbbell type to $\mathrm{Na}^{+}_{(00\frac{1}{2})}$, was observed only transiently in the parallel tempering runs and at higher temperatures (see Sec. III D 1). Such a dumbbell configuration is rare for ionic crystals due to electrostatic repulsion, but the large cavities of the feldspar framework seem to allow for this extra ion. The two Na^{+} ions lie outside the (010) plane spanned by the other sodiums. They are only 2.67 Å apart but have a comparable separation to their next-nearest neighbors as conventionally occupied Na sites. We also initialized a supercell with a sodium interstitial between two neighboring Na sites inside the folded eight-membered ring as was suggested by Behrens and coworkers [24]. However, this configuration was unstable and reconfigured to the dumbbell configuration during relaxation. The final defect we discuss is the sodium vacancy V^{-}_{Na} pictured in Fig. 1(d).

The conventional unit cell of Na-feldspar contains four formula units of $\mathrm{NaAlSi_3O_8}$ in a $C\bar{1}$ space group. A single formula unit supports only half of one $(0, 0, \frac{1}{2})$-site, whereas the dumbbell and vacancy can appear once for every sodium site. The conventional unit cell therefore supports 2 $(0, 0, \frac{1}{2})$ sites, four vacancy sites, and four dumbbell sites, each of them equivalent up to symmetry, respectively. We convinced ourselves of this explicitly for the dumbbell configuration and noticed that its axis remains the same on all possible locations. This implies that the two Na^{+} are equidistant to the center of inversion, which is situated in the middle of the eight-membered ring of tetrahedrons.

TABLE IV. Defect formation energies at 0 K for various defects after full ionic and volumetric relaxation. The defect energies were calculated according to Eq. (1) using the internal energy per atom of sodium bcc, $\mu_{Na} = -1.31$ eV, and a valence band maximum of $\epsilon_{\mathrm{VBM}} = 1.18$ eV, both determined in GGA. The Fermi level was set at the VBM, $\Delta E_{\mathrm{FL}} = 0$. The defect energy in the last row is that of the lowest energy Frenkel pair in the $2 \times 2 \times 2$ system resulting from summation of the energies in rows 1 and 3.

			Formation energies E_{form} [eV]			
			GGA		NNP	
Defect type	System	q	w/o	w/corr	w/o	w/corr
V^{-}_{Na}	2×2×2	−1	5.11	5.29	4.91	5.20
V^{-}_{Na}	2×1×2	−1	5.03	5.32	4.91	5.21
$\mathrm{Na}^{+}_{\mathrm{DB}}$	2×2×2	+1	−3.34	−3.16	−3.38	−3.13
$\mathrm{Na}^{+}_{(00\frac{1}{2})}$	2×2×2	+1	−3.00	−2.82	−3.10	−2.83
$\mathrm{Na}^{+}_{(00\frac{1}{2})}$	2×1×2	+1	−3.06	−2.79	−3.08	−2.81
$V^{-}_{\mathrm{Na}} + \mathrm{Na}^{+}_{\mathrm{DB}}$	2×2×2	+0	1.87	–	1.49	2.03
$V^{-}_{\mathrm{Na}} + \mathrm{Na}^{+}_{(00\frac{1}{2})}$	2×2×2	+0	2.27	–	1.79	2.35
Lowest energy Frenkel pair		+0	1.77	2.13	1.53	2.07

In Table IV we show the formation energies calculated for the defects in individual supercells as well as in systems containing both interstitial and vacancy defects together. The defect energies, calculated according to Eq. (1), were obtained for GGA, GGA including electrostatic corrections, the NNP committee trained on a reference without corrections (NNPw/o), and the NNP committee trained on a reference including corrections (NNPw/corr). The KO finite-size charge correction for the charged defects is relevant in the $2\times1\times2$ and only marginally less so in the $2\times2\times2$ system. The corrected formation energy does, however, seem to be converged rather well already in the $2\times2\times2$ system, decreasing only by 0.03 eV compared to the smaller system for both V^{-}_{Na} and $\mathrm{Na}^{+}_{(00\frac{1}{2})}$.

To calculate the defect energy according to Eq. (1) we use the chemical potential of sodium bcc computed at $T = 0$ and $P = 0$ with GGA. The electron energy at the valence band maximum, ϵ_{VBM}, of the perfect feldspar crystal was also determined with GGA under the same conditions. Note that in Ref. [71], GGA formation energies of sodium cation vacancies were computed without separating elemental and electronic contributions to the formation energy. Instead, the authors used the energy of a charged sodium ion in vacuum as reference, resulting in a defect formation energy that is 9 eV higher than the corresponding energy shown in Table IV.

The necessity of including NNPw/o and the NNPw/corr in this study becomes apparent when looking at the

TABLE V. Defect formation energies calculated with GGA without altering the number of electrons in the supercells.

Defect type	System	q	E_{form} [eV]
V^0_{Na}	2×2×2	+0	5.15
$\mathrm{Na}^0_{\mathrm{DB}}$	2×2×2	+0	1.53
$\mathrm{Na}^0_{(00\frac{1}{2})}$	2×2×2	+0	1.91
$\mathrm{Na}^0_{(00\frac{1}{2})}$	2×1×2	+0	1.92
Lowest energy Frenkel pair		+0	6.68

defect formation energies shown in the rightmost columns of Table IV. Generally, NNPw/o and NNPw/corr seem to reproduce the uncorrected and corrected DFT reference, respectively. The precision at which this is accomplished, however, favors NNPw/corr. In particular, for the formation energy of the Frenkel pair, shown in the last row of Table IV, NNPw/corr predicts a value quite close to the corrected reference, while NNPw/o predicts neither the uncorrected energy nor the corrected one with acceptable precision. Note that this formation energy of the Frenkel pair is consistent with the upper limit of ~2.4 eV of the enthalpic contribution to the formation free energy, which was deduced by El Maanaoui and coworkers [9] using ionic conductivity measurements in K-rich feldspar. The need for corrections is most visible in the defect formation energy of the Frenkel pairs in a single supercell, ($V^-_{\mathrm{Na}} + \mathrm{Na}^+_{\mathrm{DB}}$) and ($V^-_{\mathrm{Na}} + \mathrm{Na}^+_{(00\frac{1}{2})}$). As the Frenkel defect pair has no total charge, no charge correction is needed in this case. However, due to the finite size of the cell there remains an attraction between the interstitial defect and the vacancy, which decreases the formation energy compared to the sum of formation energies of V^-_{Na} and $\mathrm{Na}^+_{\mathrm{DB}}$ or $\mathrm{Na}^+_{(00\frac{1}{2})}$. In both cases, the NNPw/corr formation energy is closer to the reference than the NNPw/o result. Since no electrostatic correction needs to be applied in calculating the single Frenkel pair, and no configuration of a Frenkel pair in a single system was included in the training data, the good agreement of the NNPw/corr corroborates the validity of the electrostatic correction and indicates that it is a necessary ingredient in the construction of the training set.

To ensure that we correctly identified the lowest energy charge state of the Frenkel pair defect, we also calculated the defect formation energies without altering the numbers of electrons and listed these energies in Table V. The last row shows the sum of uncharged V^0_{Na} and $\mathrm{Na}^0_{\mathrm{DB}}$, which corresponds to a Frenkel pair without charge transfer between vacancy and interstitial. The formation energy of this Frenkel pair is much higher than its counterpart with charge transfer shown in the last row of Table IV. Since the latter is also similar in value to the direct Frenkel pair $V^-_{\mathrm{Na}} + \mathrm{Na}^+_{\mathrm{DB}}$ in the single supercell, we conclude that it is the appropriate lowest energy charge state.

The energies shown in Tables V and IV hold information on the transitions between charge states. The difference in formation energy of the interstitial in its neutral and charged state is 4.69 eV in the case of the dumbbell and 4.73 eV in the case of $\mathrm{Na}^+_{(00\frac{1}{2})}$. An optical transition ($\mathrm{Na}^0_{\mathrm{DB}} + h \longrightarrow \mathrm{Na}^+_{\mathrm{DB}} + \hbar\omega$) with h being a hole in the valence band would yield a photon with an energy of 4.65 eV, where slight dissimilarities in the local lattice relaxations of $\mathrm{Na}^0_{\mathrm{DB}}$ and $\mathrm{Na}^+_{\mathrm{DB}}$ are taken into account. Possibly this transition is related to a prominent peak in a recent XEOL spectrum of Na-rich feldspar at 4.5 to 4.3 eV (for 300 to 100 K) that has not been categorized yet [72]. Moreover, Garcia and coworkers [73] have detected a peak at 4.3 eV and speculated that it originates from Na^+ at interfaces. Finally, a peak is also visible at 4.5 eV in the phosphorescence spectrum of Na-feldspar [74]. An argument against a connection between $\mathrm{Na}^0_{\mathrm{DB}} \longrightarrow \mathrm{Na}^+_{\mathrm{DB}}$ and those peaks is that the latter study also reports a small peak at 4.4 eV in the phosphorescence spectra of two out of four specimens of K-rich feldspar. All these systems, however, contain also some amount of Na (as do all natural occurring alkali feldspars), and we suspect that in alkali feldspars of any composition, the dumbbell defect should be the most favorable interstitial defect as both K-K dumbbells and Na-K dumbbells would be sterically unfavorable compared to $\mathrm{Na}^+_{\mathrm{DB}}$.

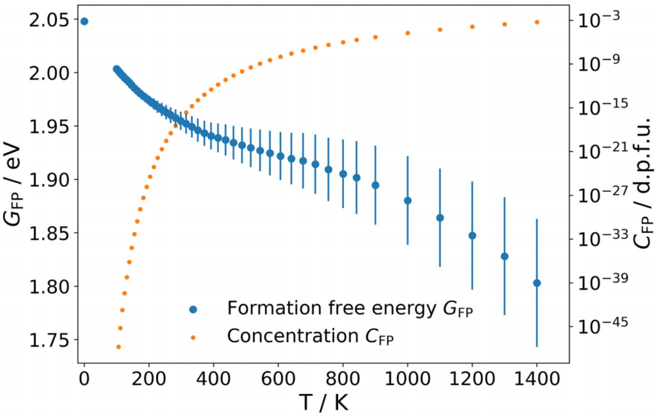

FIG. 5. Formation free energy G_{FP} with error bars of the Frenkel pair as a function o temperature T. The estimation of the error bars is described in the Supplemental Material [77]. Also shown is the resulting defect concentration C_{FP} obtained by applying Eq. (3). Defect concentrations are given in defects per formula unit (d.p.f.u.).

D. Finite temperature behavior

1. *Free energy of defect formation*

Using thermodynamic integration starting from a harmonic reference model we calculated the free energies at finite temperatures and atmospheric pressure for a pristine system, a system containing a vacancy V^-_{Na}, and a system containing an interstitial Na^+_i. Details of the thermodynamic integration procedure, combined with parallel tempering, and the resulting free energies are provided in the Supplemental Material [77]. Based on these individual free energies we determined the free energy of formation of the Frenkel pair as a function of temperature

$$G_{\mathrm{FP}} = G_{V^-_{\mathrm{Na}}} + G_{\mathrm{Na}^+_i} - 2G_{\mathrm{pristine}},$$

which is plotted in Fig. 5. Interestingly, the free energy decreases monotonically with increasing temperature, but goes through an inflection point at around 650 K. Below this temperature the free energy of formation decreases in a convex

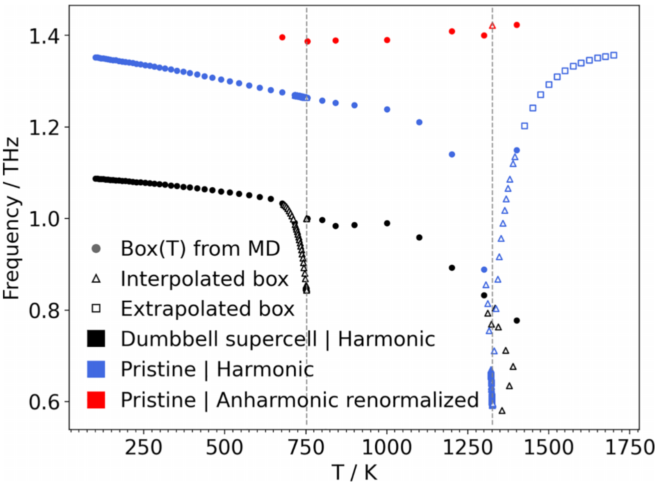

FIG. 6. The lowest normal mode frequency at the Γ point. Here anharmonic renormalization refers to normal-mode-decomposition [53]. The first minimum at 751.91 K is related to a discontinuity in the orientational axis of the dumbbell. The soft mode at 1325.60 K disappears when including anharmonic effects.

fashion, and above it it decreases concavely. Since $S = -\frac{dG}{dT}$, this implies a minimum of the formation entropy.

To investigate the origin of the inflection point in the defect formation energy we computed the relative frequency of the two possible interstitial defect states, $\mathrm{Na}^+_{\mathrm{DB}}$ and $\mathrm{Na}^+_{(00\frac{1}{2})}$. The thermodynamic integration over temperature allows the defect to sample both of these states. Using an algorithm that can discern between the $\mathrm{Na}^+_{\mathrm{DB}}$ and the $\mathrm{Na}^+_{(00\frac{1}{2})}$ states [75], we determined the relative concentration that the latter exhibited during the parallel tempering run. The fraction of $\mathrm{Na}^+_{(00\frac{1}{2})}$ ranges from 0.6% at 1400 K and about 0.02% at 1000 K to 0% below 1000 K. The $\mathrm{Na}^+_{(00\frac{1}{2})}$ state did therefore not have any contribution to the formation free energy below 1000 K and cannot be the origin of the inflection. The relative concentration as a function of T can be found in the Supplemental Maerial Fig. S-9 [77].

2. Discontinuity in the dumbbell orientation and a dynamical instability

Further insights into the nature of the dumbbell defect can be obtained by analyzing the normal mode frequencies of the system with and without defect. In Fig. 6 we show the lowest normal mode frequency at the Γ point of systems containing a dumbbell and of the pristine crystal as a function of temperature. We calculated the normal mode frequencies using the harmonic approximation or normal-mode decomposition, as described in Sec. II E, for the box dimensions corresponding to the respective temperatures (cf. Fig. 4). The box dimensions as a function of temperature were determined from parallel tempering simulations. Close to the instability temperature discussed below additional box sizes were obtained by interpolation and at higher temperature by extrapolation.

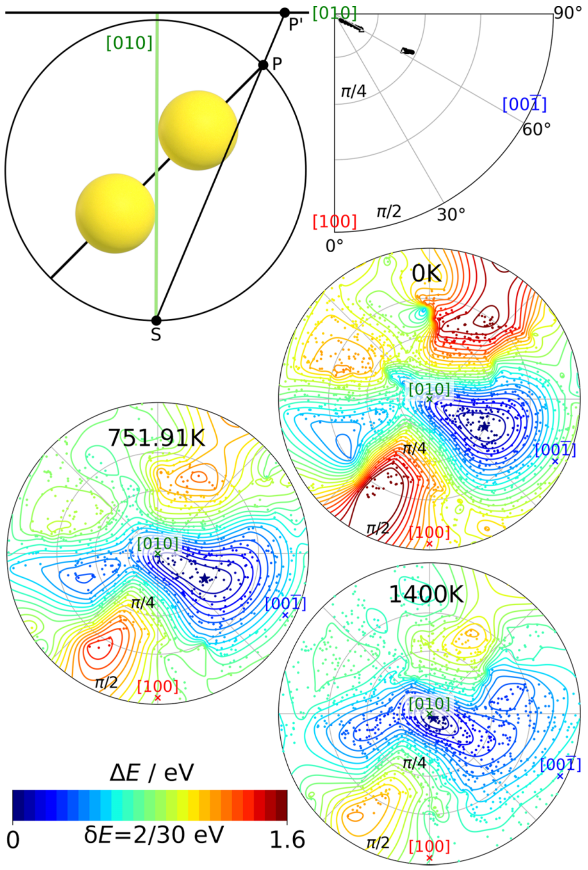

FIG. 7. The orientation of the dumbbell axis is shown using a stereographic projection, visualized in the upper left. To obtain this projection, the axis at P which lives on the upper hemisphere is mapped into the point P' of the image plane. The [010] direction is kept at 0 rad latitude and the [100] at 0° longitude. In the upper right panel, the axis orientation corresponding to the energy minimum at all temperatures of Fig. 6 is plotted, and the discontinuity in latitude occurring at 751.91 K is evident. The lower part shows the potential energy landscapes sampled for different box dimensions. The axis orientation corresponding to the energy minimum is indicated by a star.

In the system with the dumbbell, at a temperature of about 752 K a frequency vanishes and reappears at a different value. Such a discontinuity implies that a minimum in the potential energy landscape disappears, after which the system relaxes to a different minimum. Since we do not observe the same discontinuity in the pristine system, we conclude that this effect is related to a mechanical instability of the dumbbell defect.

A closer analysis reveals that the instability at 752 K is related to the orientation of the axis of the dumbbell. Figure 7 (upper right) shows this axis at the potential energy minimum for all box dimensions in a stereographic projection. At 0 K it has an almost 45° angle to the [010] direction [cf. Fig. 1(c)]. With increasing temperature this angle slightly decreases, and at 752 K it jumps by about 22.5°. Upon further temperature increase the angle decreases to almost 0° at 1400 K.

The lower parts of Fig. 7 show the potential energy landscape as a function of the axis orientation for different

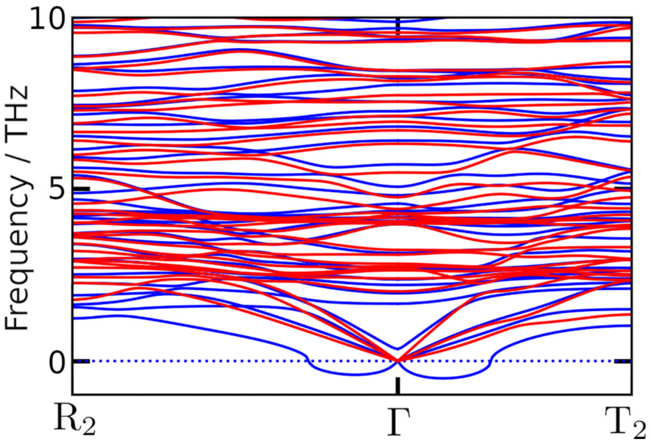

FIG. 8. Phonon bandstructure in the harmonic approximation (blue) and with anharmonicity included using normal-mode decomposition (red) at 1325.60 K. Only a step of the band path suggested in [76] is shown. The complete band structure is included in the Supplemental Material [77].

temperatures. To determine these energy landscapes, we held the axis of the two Na^+ in the dumbbell fixed at random values and relaxed all other degrees of freedom (including the distance of the dumbbell atoms to each other). Only samples with a separation of the two Na^+ smaller than 3.8 Å are counted as dumbbell defects. Configurations with a larger separation correspond to a $\mathrm{Na}^+_{\mathrm{DB}}$ at a different alkali site or even an $\mathrm{Na}^+_{(00\frac{1}{2})}$ defect.

Across all box dimensions the dumbbell axis shows high anisotropy and energetically favors orientations between [010] and [$00\bar{1}$]. Orientations between [010] and [100] are energetically much more costly. As the box dimensions increase with temperature, the well between [010] and [$00\bar{1}$] flattens and at 752 K a new minimum emerges. As only one alkali site is considered, the potential energy landscape would have to be appropriately inverted for an $\mathrm{Na}^+_{\mathrm{DB}}$ at the alternative alkali site.

The necessity for using thermodynamic integration to incorporate anharmonic effects in the free energies of Fig. 5 is evidenced by the appearance of a soft mode at about 1325 K in the harmonic approximation in both pristine and interstitial systems, as shown in Fig 6. Below 1300 K the crystal is dynamically stable, but between 1300–1400 K an optical mode almost vanishes and an acoustic band exhibits a dynamical instability. An excerpt of the band structure at 1325.60 K is shown in Fig. 8. Curiously, the crystal regains its harmonic stability if we extrapolate the box dimensions beyond 1400 K. The dynamical instability in the band structure disappears completely after renormalizing the bands by incorporating finite temperature effects using normal-mode decomposition. This shows that the dynamical instability is a harmonic artifact and that anharmonic effects are essential in modeling Na-feldspar at these high temperatures.

IV. CONCLUSIONS

In this work we presented an NNP, purpose-built for Na-feldspar (albite) and its defects, and demonstrated its applicability to simulate this system by predicting relevant physical properties. In constructing the potential we made use of on-the-fly machine learning initially and then expanded the dataset using an NNP committee machine. This way to proceed required less human intervention than typically needed for NNPs and should be widely applicable.

We have shown that electrostatic corrections need to be included into the training dataset for the NNP. This is particularly important when defect formation energies are of interest. Including corrections after training produces a potential that cannot transfer to systems that are made up of multiple defects that neutralize each other, such as Frenkel pairs in Na-feldspar.

Based on our NNP, we have found a new kind of interstitial defect in the dumbbell configuration $\mathrm{Na}^+_{\mathrm{DB}}$, where two Na^+ cations share a single site on the alkali sublattice. This defect is the energetically most favorable, but at elevated temperatures transitions occur between $\mathrm{Na}^+_{\mathrm{DB}}$ and the less favorable $\mathrm{Na}^+_{(00\frac{1}{2})}$-interstitial, which was observed previously. These different defect configurations as well as the instability in the axis orientation of the dumbbell defect might affect the free energy of formation of the Frenkel pair, which we found to go through an inflection at elevated temperatures.

A promising future application of the NNP develped in our work will be the direct determination of diffusion coefficients of defects using MD. Combined with the free energy of defect formation, it will be possible to compare these with experimentally determined tracer diffusion coefficients and elucidate the underlying diffusion mechanism. The latter is key for understanding the formation of exsolution microsctructures in alkali feldspar used in reconstructing the thermal history of magmatic and metamorphic rocks [2,3]. A second topic of interest is the extension of this NNP potential to include also potassium feldspar to study mixed systems of both sodium and potassium feldspar, if possible including disorder in the sites occupied by silicon and aluminum. These points will be addressed in future research.

The training and test data, the NNPw/corr, a template for molecular dynamics as well as LAMMPS-DATA configurations of the pristine, $\mathrm{Na}^+_{(00\frac{1}{2})}$, $\mathrm{Na}^+_{\mathrm{DB}}$, $\mathrm{V}^-_{\mathrm{Na}}$, $\mathrm{V}^-_{\mathrm{Na}} + \mathrm{Na}^+_{\mathrm{DB}}$ and $\mathrm{V}^-_{\mathrm{Na}} + \mathrm{Na}^+_{(00\frac{1}{2})}$ systems are openly available through the Zenodo repository [78].

ACKNOWLEDGMENTS

We would like to thank Ferenc Karsai and the VASP team for supporting us in using the on-the-fly methododology in its then development stage. We further acknowledge financial support from the Austrian Science Fund (FWF) through Grant-DOI 10.55776/I4404 and through Grant-DOI 10.55776/F81. The computational results presented were achieved using the Vienna Scientific Cluster (VSC).

[1] M. Dondi, Feldspathic fluxes for ceramics: Sources, production trends and technological value, Res. Conserv. Recycling **133**, 191 (2018).

[2] I. Parsons, J. D. F. Gerald, and M. R. Lee, Review. Routine characterization and interpretation of complex alkali feldspar intergrowths, Am. Mineral. **100**, 1277 (2015).

[3] R. Abart, E. Petrishcheva, R. Wirth, and D. Rhede, Exsolution by spinodal decomposition II: Perthite formation during slow cooling of anatexites from Ngoronghoro, Tanzania, Am. J. Sci. **309**, 450 (2009).

[4] A. Kiselev, F. Bachmann, P. Pedevilla, S. J. Cox, A. Michaelides, D. Gerthsen, and T. Leisner, Active sites in heterogeneous ice nucleation—The example of K-rich feldspars, Science **355**, 367 (2017).

[5] E. Petrishcheva, R. Abart, A. K. Schäffer, G. Habler, and D. Rhede, Sodium-potassium interdiffusion in potassium-rich alkali feldspar I: Full diffusivity tensor at 850 °C, Am. J. Sci. **314**, 1284 (2014).

[6] E. Petrishcheva, L. Tiede, D. Heuser, H. Hutter, G. Giester, and R. Abart, Multicomponent diffusion in ionic crystals: Theoretical model and application to combined tracer- and interdiffusion in alkali feldspar, Phys. Chem. Miner. **47**, 35 (2020).

[7] F. Hergemöller, M. Wegner, M. Deicher, H. Wolf, F. Brenner, H. Hutter, R. Abart, and N. A. Stolwijk, Potassium self-diffusion in a K-rich single-crystal alkali feldspar, Phys. Chem. Miner. **44**, 345 (2017).

[8] F. Wilangowski and N. A. Stolwijk, Vacancy-related diffusion correlation effects in a simple cubic random alloy and on the Na-K sublattice of alkali feldspar, Philos. Mag. **95**, 2277 (2015).

[9] H. El Maanaoui, F. Wilangowski, A. Maheshwari, H.-D. Wiemhöfer, R. Abart, and N. A. Stolwijk, Ionic conductivity in gem-quality single-crystal alkali feldspar from the Eifel: Temperature, orientation and composition dependence, Phys. Chem. Miner. **43**, 327 (2016).

[10] F. Wilangowski, R. Abart, S. V. Divinski, and N. A. Stolwijk, Radiotracer experiments and Monte Carlo simulations of sodium diffusion in alkali feldspar: Evidence against the vacancy mechanism, Defect Diffusion Forum **363**, 79 (2015).

[11] F. Wilangowski and N. A. Stolwijk, Monte Carlo simulation of diffusion and ionic conductivity in a simple cubic random alloy via the interstitialcy mechanism, J. Phys.: Condens. Matter **27**, 505401 (2015).

[12] F. Wilangowski and N. A. Stolwijk, A Monte Carlo study of ionic transport in a simple cubic random alloy via the interstitialcy mechanism: Effects of non-collinear and direct interstitial jumps, Philos. Mag. **97**, 108 (2017).

[13] C. R. A. Catlow, *Modelling of Structure and Reactivity in Zeolites* (Academic Press, Cambridge, Massachusetts, 1992).

[14] A. Jones, M. S. Islam, M. Mortimer, and D. Palmer, Alkali ion migration in albite and K-feldspar, Phys. Chem. Miner. **31**, 313 (2004).

[15] P. Kaercher, B. Militzer, and H. R. Wenk, Ab initio calculations of elastic constants of plagioclase feldspars, Am. Mineral. **99**, 2344 (2014).

[16] J. Behler and M. Parrinello, Generalized neural-network representation of high-dimensional potential-energy surfaces, Phys. Rev. Lett. **98**, 146401 (2007).

[17] A. P. Bartók, M. C. Payne, R. Kondor, and G. Csányi, Gaussian approximation potentials: The accuracy of quantum mechanics, without the electrons, Phys. Rev. Lett. **104**, 136403 (2010).

[18] O. T. Unke, S. Chmiela, H. E. Sauceda, M. Gastegger, I. Poltavsky, K. T. Schütt, A. Tkatchenko, and K. R. Müller, Machine learning force fields, Chem. Rev. **121**, 10142 (2021).

[19] P. Friederich, F. Häse, J. Proppe, and A. Aspuru-Guzik, Machine-learned potentials for next-generation matter simulations, Nat. Mater. **20**, 750 (2021).

[20] A. Omranpour, P. Montero De Hijes, J. Behler, and C. Dellago, Perspective: Atomistic simulations of water and aqueous systems with machine learning potentials, J. Chem. Phys. **160**, 170901 (2024).

[21] M. Mińkowski, K. Hummer, and C. Dellago, Cation interstitial diffusion in lead telluride and cadmium telluride studied by means of neural network potential based molecular dynamics simulations, J. Phys.: Condens. Matter **33**, 015901 (2021).

[22] P. M. Piaggi, A. Selloni, A. Z. Panagiotopoulos, R. Car, and P. G. Debenedetti, A first-principles machine-learning force field for heterogeneous ice nucleation on microcline feldspar, Faraday Discuss. **249**, 98 (2024).

[23] J. P. Perdew, K. Burke, and M. Ernzerhof, Generalized gradient approximation made simple, Phys. Rev. Lett. **77**, 3865 (1996).

[24] H. Behrens, W. Johannes, and H. Schmalzried, On the mechanisms of cation diffusion processes in ternary feldspars, Phys. Chem. Miner. **17**, 62 (1990).

[25] R. Petrovic, Diffusion of alkali ions in alkali feldspars, in *The Feldspars: Proceedings of a NATO Advanced Study Institute*, edited by W. S. MacKenzie and J. Zussman (Manchester University Press, 1974), pp. 174–182.

[26] G. Kresse and J. Hafner, Ab initio molecular dynamics for liquid metals, Phys. Rev. B **47**, 558 (1993).

[27] G. Kresse and J. Furthmüller, Efficient iterative schemes for ab initio total-energy calculations using a plane-wave basis set, Phys. Rev. B **54**, 11169 (1996).

[28] G. Kresse and J. Furthmüller, Efficiency of ab-initio total energy calculations for metals and semiconductors using a plane-wave basis set, Comput. Mater. Sci. **6**, 15 (1996).

[29] G. Kresse and D. Joubert, From ultrasoft pseudopotentials to the projector augmented-wave method, Phys. Rev. B **59**, 1758 (1999).

[30] T. Armbruster, H. B. Buergi, M. Kunz, E. Gnos, S. Broenniman, and C. Lienert, Variation of displacement parameters in structure refinements of low albite, Am. Mineral. **75**, 135 (1990).

[31] S. B. Zhang and J. E. Northrup, Chemical potential dependence of defect formation energies in GaAs: Application to Ga self-diffusion, Phys. Rev. Lett. **67**, 2339 (1991).

[32] C. Freysoldt, B. Grabowski, T. Hickel, J. Neugebauer, G. Kresse, A. Janotti, and C. G. Van de Walle, First-principles calculations for point defects in solids, Rev. Mod. Phys. **86**, 253 (2014).

[33] Y. Kumagai and F. Oba, Electrostatics-based finite-size corrections for first-principles point defect calculations, Phys. Rev. B **89**, 195205 (2014).

[34] M. Gajdoš, K. Hummer, G. Kresse, J. Furthmüller, and F. Bechstedt, Linear optical properties in the projector-augmented wave methodology, Phys. Rev. B **73**, 045112 (2006).

[35] M. Arrigoni and G. K. Madsen, Spinney: Post-processing of first-principles calculations of point defects in semiconductors with Python, Comput. Phys. Commun. **264**, 107946 (2021).

[36] G. Olhoeft, Electrical properties of rocks, in *Physical Properties of Rocks and Minerals*, edited by Y. Touloukian, W. Judd, and R. Roy (Hemisphere Publications, 1989), pp. 257–329.

[37] A. Singraber, T. Morawietz, J. Behler, and C. Dellago, Parallel multistream training of high-dimensional neural network potentials, J. Chem. Theory Comput. **15**, 3075 (2019).

[38] A. Singraber, J. Behler, and C. Dellago, Library-based LAMMPS implementation of high-dimensional neural network potentials, J. Chem. Theory Comput. **15**, 1827 (2019).

[39] A. P. Thompson, H. M. Aktulga, R. Berger, D. S. Bolintineanu, W. M. Brown, P. S. Crozier, P. J. in 't Veld, A. Kohlmeyer, S. G. Moore, T. D. Nguyen *et al.*, LAMMPS—A flexible simulation tool for particle-based materials modeling at the atomic, meso, and continuum scales, Comput. Phys. Commun. **271**, 108171 (2022).

[40] L. Kývala, A. Angeletti, C. Franchini, and C. Dellago, Diffusion and coalescence of phosphorene monovacancies studied using high-dimensional neural network potentials, J. Phys. Chem. C **127**, 23743 (2023).

[41] C. Schran, K. Brezina, and O. Marsalek, Committee neural network potentials control generalization errors and enable active learning, J. Chem. Phys. **153**, 104105 (2020).

[42] G. Imbalzano, Y. Zhuang, V. Kapil, K. Rossi, E. A. Engel, F. Grasselli, and M. Ceriotti, Uncertainty estimation for molecular dynamics and sampling, J. Chem. Phys. **154**, 074102 (2021).

[43] D. H. Wolpert, Stacked generalization, Neural Networks **5**, 241 (1992).

[44] A. Krogh and J. Vedelsby, Neural network ensembles, cross validation, and active learning, in *Advances in Neural Information Processing Systems*, Vol. 7, edited by G. Tesauro, D. Touretzky, and T. Leen (MIT Press, 1994), pp. 231–238.

[45] N. Ueda and R. Nakano, Generalization error of ensemble estimators, in *Proceedings of International Conference on Neural Networks (ICNN'96)*, Vol. 1 (IEEE, Picataway, NJ, 1996), pp. 90–95.

[46] R. Jinnouchi, F. Karsai, and G. Kresse, On-the-fly machine learning force field generation: Application to melting points, Phys. Rev. B **100**, 014105 (2019).

[47] R. Jinnouchi, J. Lahnsteiner, F. Karsai, G. Kresse, and M. Bokdam, Phase transitions of hybrid perovskites simulated by machine-learning force fields trained on the fly with Bayesian inference, Phys. Rev. Lett. **122**, 225701 (2019).

[48] G. Imbalzano and M. Ceriotti, Modeling the Ga/As binary system across temperatures and compositions from first principles, Phys. Rev. Mater. **5**, 063804 (2021).

[49] Y. Zuo, C. Chen, X. Li, Z. Deng, Y. Chen, J. Behler, G. Csányi, A. V. Shapeev, A. P. Thompson, M. A. Wood, and S. P. Ong, Performance and cost assessment of machine learning interatomic potentials, J. Phys. Chem. A **124**, 731 (2020).

[50] Y. Le Page and P. Saxe, Symmetry-general least-squares extraction of elastic data for strained materials from *ab initio* calculations of stress, Phys. Rev. B **65**, 104104 (2002).

[51] A. Togo and I. Tanaka, First principles phonon calculations in materials science, Scr. Mater. **108**, 1 (2015).

[52] T. Sun, D.-B. Zhang, and R. M. Wentzcovitch, Dynamic stabilization of cubic $CaSiO_3$ perovskite at high temperatures and pressures from *ab initio* molecular dynamics, Phys. Rev. B **89**, 094109 (2014).

[53] A. Carreras, A. Togo, and I. Tanaka, Dynaphopy: A code for extracting phonon quasiparticles from molecular dynamics simulations, Comput. Phys. Commun. **221**, 221 (2017).

[54] H. Mehrer, *Diffusion in Solids: Fundamentals, Methods, Materials, Diffusion-Controlled Processes*, Springer Series in Solid-State Sciences (Springer, Berlin, 2007), pp. 69–93.

[55] B. Cheng and M. Ceriotti, Computing the absolute Gibbs free energy in atomistic simulations: Applications to defects in solids, Phys. Rev. B **97**, 054102 (2018).

[56] V. Kapil, M. Rossi, O. Marsalek, R. Petraglia, Y. Litman, T. Spura, B. Cheng, A. Cuzzocrea, R. H. Meißner, D. M. Wilkins *et al.*, i-pi 2.0: A universal force engine for advanced molecular simulations, Comput. Phys. Commun. **236**, 214 (2019).

[57] T. Okabe, M. Kawata, Y. Okamoto, and M. Mikami, Replica-exchange Monte Carlo method for the isobaric-isothermal ensemble, Chem. Phys. Lett. **335**, 435 (2001).

[58] J. F. Schairer and N. L. Bowen, The system Na_2O-Al_2O_3-SiO_2, Am. J. Sci. **254**, 129 (1956).

[59] E. D. Dietz, T. Baak, and H. H. Blau, The superheating of an albite feldspar, Z. Kristallogr.-Cryst. Mater. **132**, 340 (1970).

[60] J. P. Greenwood and P. C. Hess, Congruent melting kinetics of albite: Theory and experiment, J. Geophys. Res.: Solid Earth **103**, 29815 (1998).

[61] B. Grabowski, L. Ismer, T. Hickel, and J. Neugebauer, *Ab initio* up to the melting point: Anharmonicity and vacancies in aluminum, Phys. Rev. B **79**, 134106 (2009).

[62] A. Glensk, B. Grabowski, T. Hickel, and J. Neugebauer, Breakdown of the arrhenius law in describing vacancy formation energies: The importance of local anharmonicity revealed by *ab initio* thermodynamics, Phys. Rev. X **4**, 011018 (2014).

[63] J. M. Brown, E. H. Abramson, and R. J. Angel, Triclinic elastic constants for low albite, Phys. Chem. Miner. **33**, 256 (2006).

[64] T. Ryzhova, Elastic properties of plagioclase, Bull. Acad. Sci. USSR, Geophys. Ser. **7**, 633 (1964).

[65] A. Benisek, E. Dachs, and H. Kroll, Thermochemistry of the alkali feldspars: Calorimetric study of the entropy relations in the low albite-low microcline series, Am. Mineral. **99**, 76 (2014).

[66] E. Salje, B. Kuscholke, B. Wruck, and H. Kroll, Thermodynamics of sodium feldspar II: Experimental results and numerical calculations, Phys. Chem. Miner. **12**, 99 (1985).

[67] H. Kroll, Thermal expansion of alkali feldspars, in *Feldspars and Feldspathoids: Structures, Properties and Occurrences*, edited by W. L. Brown (Springer Netherlands, Dordrecht, 1984), pp. 163–205.

[68] M. Gottschalk, Internally consistent thermodynamic data for rock-forming minerals in the system SiO_2-TiO_2-Al_2O_3-CaO-MgO-FeO-K_2O-Na_2O-H_2O-CO_2, Eur. J. Mineral. **9**, 175 (1997).

[69] T. J. B. Holland and R. Powell, An internally consistent thermodynamic data set for phases of petrological interest, J. Metamorph. Geol. **16**, 309 (1998).

[70] M. Tribaudino, R. J. Angel, F. Cámara, F. Nestola, D. Pasqual, and I. Margiolaki, Thermal expansion of plagioclase feldspars, Contrib. Mineral. Petrol. **160**, 899 (2010).

[71] S. Lowitzer, D. J. Wilson, B. Winkler, V. Milman, and J. D. Gale, Defect properties of albite, Phys. Chem. Miner. **35**, 129 (2008).

[72] N. R. J. Poolton and R. H. Kars, On the linewidth of luminescence emission bands in alkali feldspars, Radiation Measure. **158**, 106848 (2022).

[73] J. Garcia-Guinea, P. Townsend, L. Sanchez-Munoz, and J. Rojo, Ultraviolet-blue ionic luminescence of alkali feldspars from bulk and interfaces, Phys. Chem. Miner. **26**, 658 (1999).

[74] M. R. Baril and D. J. Huntley, Infrared stimulated luminescence and phosphorescence spectra of irradiated feldspars, J. Phys.: Condens. Matter **15**, 8029 (2003).

[75] A. Gorfer, R. Abart, and C. Dellago, Mechanism and kinetics of sodium diffusion in Na-feldspar from neural network based atomistic simulations, arXiv:2405.19008.

[76] Y. Hinuma, G. Pizzi, Y. Kumagai, F. Oba, and I. Tanaka, Band structure diagram paths based on crystallography, Comput. Mater. Sci. **128**, 140 (2017).

[77] See Supplemental Material at http://link.aps.org/supplemental/10.1103/PhysRevMaterials.8.073602 for details on the electrostatic correction, the thermodynamic integration and the normal mode decomposition.

[78] A. Gorfer, R. Abar, and C. Dellago, “Structure and thermodynamics of defects in Na-feldspar from a neural network potential (2024)” [Data set], https://doi.org/10.5281/zenodo.10630971.